Radiative–Convective Equilibrium with Explicit Two-Dimensional Moist Convection

ISAAC M. HELD AND RICHARD S. HEMLER

Geophysical Fluid Dynamics Laboratory/NOAA, Princeton University, Princeton, New Jersey

V. RAMASWAMY

Program in Atmospheric and Oceanic Sciences, Princeton University, Princeton, New Jersey

(Manuscript received 7 December 1992, in final form 29 April 1993)

ABSTRACT

Radiative–convective statistical equilibria are obtained using a two-dimensional model in which radiative transfer is interactive with the predicted moisture and cloud fields. The domain is periodic in x, with a width of 640 km, and extends from the ground to 26 km. The lower boundary is a fixed-temperature water-saturated surface. The model produces a temperature profile resembling the mean profile observed in the tropics. A number of integrations of several months' duration are described in this preliminary examination of the model's qualitative behavior.

The model generates a QBO-like oscillation in the x-averaged winds with an apparent period of ~60 days. This oscillation extends into the troposphere and influences the convective organization. In order to avoid the associated large vertical wind shears, calculations are also performed in which the x-averaged winds are constrained to vanish. The convection then evolves into a pattern in which rain falls only within a small part of the domain. The moisture field appears to provide the memory that localizes the convection.

If the vertical shears are fixed at a modest nonzero value, this localization is avoided. Comparing calculations with surface temperatures of 25° and 30°C, the planetary albedo is found to decrease with increasing temperature, primarily due to a reduction in low-level cloudiness.

1. Introduction

As computer resources have increased, some cloud modelers have moved from the investigation of individual convective cells to the study of the statistical properties of moist convection in different large-scale environments (e.g., Lipps and Hemler 1986; Tao et al. 1987; Nakajima and Matsuno 1988; Sui et al. 1993). In some cases, these studies are motivated by the desire to test closure schemes for moist convection or cloud cover in larger-scale models (Gregory and Miller 1989; Xu and Krueger 1991). In such calculations, the thermodynamic state of the atmosphere does not come into equilibrium with the convection; indeed, it is precisely the *tendency* of the large-scale temperature and moisture fields, for a given large-scale state, that is of primary interest in testing closure schemes. In contrast, in this paper we examine a model in which the moist convective turbulence and its environment come into mutual equilibrium. This equilibrium is achieved not only through the exchange of heat and moisture by the convection, but through the effect of clouds on radiative fluxes and heating rates as well.

Radiative–convective equilibrium models have proven to be invaluable in studies of climatic sensitivity. Following the classic study of Manabe and Strickler (1964), in these models one assumes the existence of the vertical heat transport needed to prevent the lapse rate from increasing beyond some prescribed value. An assumption is also required to determine the humidity profile; fixed relative humidity is the most common choice, following Manabe and Wetherald (1967). The limiting lapse rate and the relative humidity profile are typically taken from the present climatic state. One also generally assumes that the cloud amounts and optical properties are fixed, although the implications of other assumptions have been examined, as in Somerville and Remer (1984). [Ramanathan and Coakley (1978) provide a review of radiative–convective models.] Our goal in this work is to replace these assumptions with an explicit model of moist convective heat and water vapor transport and cloud formation. Some of the issues that arise in such a study are discussed by Sarachik (1978) and Betts and Ridgeway (1989).

A two-dimensional nonrotating model has been chosen so that the long integrations needed, of several months' duration, would be feasible. Some of the properties of the convection and cloud field in a statistically steady state will undoubtedly be sensitive to dimensionality. [The calculations of Lipps and Hemler

Corresponding author address: Dr. Isaac M. Held, NOAA/GFDL, Princeton University, P.O. Box 308, Princeton, NJ 08540.

(1986) suggest some of the differences to be expected in the structure of 2D and 3D moist convection.] An important role of parameter studies with such a model is the formulation of hypotheses for testing with three-dimensional models.

Our domain is periodic in the horizontal (referred to in the following as the zonal, or x) direction. The lower boundary condition is zonally uniform, the solar insolation is fixed at a tropical value, and the diurnal and seasonal cycles are ignored, so the resulting statistically steady states are presumed to be homogeneous in x and stationary in time. The surface is assumed to be water saturated, that is, ocean covered. We have chosen to fix the surface temperature in these initial experiments and to examine the sensitivity of the model to the prescribed temperature. By examining the sensitivity of the energy flux into the surface, or the net radiative flux at the top of the atmosphere, as the surface temperature is altered, one can infer much about how a model with variable surface temperature would behave.

Large-scale vertical velocities have often been imposed in models of statistically steady moist convection, since nearly all moist convection in the tropics occurs in regions of low-level convergence. In this study we have imposed no mean vertical velocity or large-scale convergence. The intention is to model a nonrotating atmosphere overlying a uniform surface and illuminated uniformly by the sun. Nakajima and Matsuno (1988) have described calculations with a similar homogeneous, two-dimensional cloud model, but without the interaction between radiative heating and the predicted cloud distribution. Their calculation emphasizes the need for a cloud model that can realistically terminate convective events through evaporative cooling.

The convection in such a horizontally homogeneous model will differ in many ways from convection in more realistic inhomogeneous environments, and results on the sensitivity of such a model are not directly relevant to the sensitivity of the global mean or the tropical climate. Inhomogeneous calculations with large-scale flows forced by convective heating will be needed to test the plausibility of hypotheses concerning climatic sensitivity. However, we believe that this homogeneous model is an interesting and fundamental starting point for studies of statistically steady moist convective turbulence.

The cloud model and the radiative transfer code utilized in these calculations are described briefly in section 2, and in more detail in the appendixes.

Being periodic in x, the model is free to generate zonal mean winds through the convergence of the vertical eddy momentum flux. Indeed, one anticipates interesting low-frequency variability in the mean winds. The quasi-biennial oscillation (QBO) in the tropical stratosphere is thought to be the result of mean flow accelerations due to the dissipation of vertically propagating waves generated by tropical convection (Lindzen and Holton 1968; Holton and Lindzen 1972). Plumb (1977) has isolated the underlying mechanism in a two-dimensional, nonrotating model in which gravity waves with both eastward and westward phase speeds are excited. One expects eastward and westward propagating waves to be generated by our model's moist convection, so a QBO-like oscillation in the model's stratosphere is a possibility. An oscillation *is* produced by this model, with some surprising characteristics, as described in section 3.

The large shears generated by this "QBO" strongly affect the structure of the model's convection, so we have also considered the consequences of suppressing this oscillation by forcing the mean zonal winds to vanish identically. In this case, the model slowly falls into a regime in which the precipitation is localized in a very small region. The convection is still episodic, but new cells continually redevelop at the same spot. These results are summarized in section 4.

By prescribing the vertical shears at a nonzero value, one eliminates the localization and still avoids the complexities introduced by the model's "QBO." Calculations are described with this third version of the model in section 5, with two values of the surface temperature (25°C and 30°C). In section 6 there is a brief comparison of the domain averaged temperature and humidity profiles generated in the calculations with localized and homogeneously distributed convection, to illustrate how these profiles are dependent on the convective organization.

2. Model description

Our starting point for these calculations is a two-dimensional version of the cloud model developed by Lipps and Hemler (1986, 1988, 1991). An elastic version of the model is used here, similar to that described by Klemp and Wilhelmson (1978), in which vertically propagating sound waves are treated implicitly. In this model the maximum allowable time step is determined by $\Delta z/W$ or $\Delta x/c$, whichever is greater. Here Δx and Δz are the horizontal and vertical grid sizes, W is the vertical velocity in the convective cores, and c is the sound speed. We have chosen a relatively large Δx, 5 km, for these calculations. This resolution is marginal for the deep convective cores of primary interest, and inadequate for explicitly resolving shallow convection, but was necessary in practice for these preliminary parameter studies. Given this Δx, we choose Δz as small as possible without impacting the time step appreciably, given our desire to resolve the small vertical scales in the cloud–radiative interactions. The value $\Delta z = 200$ m is used in the calculations that follow. Using 128 $\times$ 130 points in the x–z plane results in a domain that is 640 km $\times$ 26 km. With this choice of relatively high vertical resolution, there is little computational advantage in using an anelastic model. The model requires roughly 80 minutes of cpu time on one CRAY YMP processor per day of simulated time.

The cloud model is described more fully in appendix A. Below we highlight some features of particular importance.

- A Kessler scheme (1969), in which liquid water is divided into two categories, falling (rainwater) and nonfalling (cloud water), is supplemented by a simple falling ice phase. There is a critical cloud water concentration that is required before autoconversion into falling meteors. Preliminary calculations in which the same critical value was used for conversion into falling ice (snow) and for conversion into rain produced nearly total cloud cover at the model's tropopause. [Similar results have been obtained in short experiments with 2D and 3D models by Islam et al. (1993).] While these experiments were not run to equilibrium, we have chosen to consider instead the limiting case in which the critical value for autoconversion into snow is set to zero, so that cirrus falls out more readily. The resulting model may underestimate the role of cirrus in determining the net radiative balance and the radiative–convective equilibrium.
- A drag law is used to compute the evaporation, sensible heat flux, and stress at the surface. For the evaporation this takes the form

$$E = \rho c_d |\mathbf{v}|(r - r_s(T_s)), \qquad (1)$$

where r is the mixing ratio in the lowest model level and r_s is the saturation mixing ratio at the surface temperature T_s. For these initial calculations, we were reluctant to allow the evaporation—that is, the strength of the model's hydrologic cycle—to depend entirely on the surface wind speeds $|\mathbf{v}|$ generated by the convective model, and imposed instead a minimum value. The value of 5 m s^{-1} was chosen for $|\mathbf{v}|_{\min}$. This has more or less the same effect as the addition of a uniform mean wind of 5 m s^{-1} to the turbulent velocities generated by the model, but without the east–west asymmetry that would thereby be created. (In the presence of mean easterlies, for example, small positive eddy velocities would decrease the evaporation, while negative velocities would increase it.) Therefore, "evaporation–wind feedback" (Neelin et al. 1987; Emanuel 1987) is very much curtailed in these calculations.
- A deformation- and Richardson number–dependent subgrid-scale mixing formulation is included in the model, but, with this resolution, a well-defined mixed layer is not produced at the surface.
- A sponge layer near the model top helps absorb the vertically propagating gravity waves generated by the convection. The deviations from the zonal mean winds and potential temperatures are damped to zero linearly with the strength $\kappa = \kappa_0(z - 22\ \text{km})^2$, where κ_0 is such as to give a damping time of 500 s at the top of the model at 26 km. While we have not obtained a quantitative measure, inspection of videos of these simulations suggests that there is some residual wave reflection, particularly from the burst of waves with large vertical scales immediately following a deep convective event.

The solar and longwave radiative transfer algorithms employed are modified versions of the schemes in Ramaswamy and Kiehl (1985), and are described in appendix B. There are 56 spectral intervals in the solar spectrum. The δ-Eddington approximation (Joseph et al. 1976; Coakley et al. 1983), together with an adding scheme, is used to obtain the fluxes and heating rates in each spectral interval. In the longwave, all of the important trace gases (CO_2, CH_4, N_2O, CFC-11, and CFC-12) are considered, although the gases other than CO_2 have little influence on these calculations. The radiation algorithm treats each layer, at a given grid point, as being either clear or uniformly cloud covered. The surface has an albedo of 0.07 and an emissivity of unity. There is no diurnal cycle; the solar zenith angle is set at 53° so as to generate appropriate diurnally averaged tropical insolation. A tropical ozone profile is adopted (McClatchey et al. 1972). The liquid water (cloud plus rainwater) is lumped with the ice concentration in the radiative calculation, and the sum is treated as if it consisted of 5-μm spherical drops in both the solar and longwave spectra. The radiative heating rates are updated only every 6×10^3 s, to provide a rough balance between the computations required in the radiative and nonradiative parts of the model. This may significantly distort the cloud–radiative interactions, particularly the anvil dynamics.

Figure 1 shows the total condensed water at four times, separated by 90 min, from the calculations to be described in section 5 (with T_s = 30°C). At the earliest time, a well-defined deep convective plume has just formed. Six hours later, the plume has dissipated, leaving a cloud deck that persists for several more hours. This scene is fairly typical of the model, with scattered low-level clouds forming in the lowest few model levels, and with the debris from previous deep convective events evident in the upper troposphere (although the debris is often more extensive). Figure 2a shows the net radiative heating rate around the cloud deck in the final panel of Fig. 1. A close-up of the condensed water mixing ratio is included in Fig. 2b for easier comparison. The cooling at cloud top and the heating underneath the overhanging anvil each reach 20 K/day in this case. (An incipient, marginally resolved cloud-top instability, with scale of ~30 km, is evident in the mixing ratios.) Cooling rates at cloud top can reach values as large as 50 K/day in this model.

The initial condition for our first integration is a completely dry atmosphere and a temperature profile approximating what one would obtain from a dry convective adjustment: a dry-adiabatic layer of 6-km thickness overlain by a stable stratosphere (plus some random noise to break the zonal symmetry). The code underwent a shakedown during the spinup, and a few changes were made, so we do not stress here the char-

acteristics of the spinup, which were quite complex. We have no evidence for nonuniqueness of the statistically steady states of this model, other than that implied by the localization of the convection described in section 4.

No extra sources of noise are included; the model simply evolves freely from its initial condition, and convective events are triggered by remnants of previous events. One can question whether the absence of resolved turbulence in the boundary layer at this resolution would result in insufficient noise at low levels to trigger convection in a physically plausible manner, and this may be relevant to the results of section 4.

3. A QBO-like oscillation

Before describing the vertical structure of the temperature, humidity, and cloud variables in the resulting radiative–convective equilibrium, we focus on two intriguing features of the model, beginning with a zonal mean wind evolution that bears a qualitative resemblance to the QBO in the equatorial stratosphere.

Figure 3 shows the precipitation as a function of x and t for the final 3.6×10^6 s of an integration with $T_s = 30°C$, along with the zonal mean zonal wind as a function of height for the same period. (The total length of the integration, including spinup, is nearly 10^7 s.) The rainfall is organized into bands that correspond to propagating convective activity. For the first 6×10^5 s, the propagation is westward. Following a period of less organized convection, a pattern of eastward propagation emerges and persists for nearly 2×10^6 s. Near the end of the period shown, the convection is again disorganized, with westward movement beginning to be apparent once again. The speed of propagation is typically 5–7 m s^{-1}. The direction is clearly controlled by the low-level zonal-mean winds, which undergo a transition from negative to positive values near the time at which the direction of propagation changes sign.

The oscillation in the low-level mean winds is part of a downward-propagating wind pattern that has its largest amplitudes (>20 m s^{-1}) in the model's sponge layer above 20 km. The downward propagation is fairly steady until the winds reach the tropopause near 16 km, at which point one sees signs of more rapid descent throughout the upper troposphere, presumably due to mixing associated with the convection. Yet the remaining descent through the lower troposphere once again proceeds very steadily. Wind anomalies of opposite sign appear in the sponge layer at about the time at which penetration into the troposphere occurs. Extrapolated from the results shown, the period of this model's "QBO" is roughly 6×10^6 s.

Large shears are generated in the troposphere, as large as 10 m s^{-1} over 2 km near the surface and 30 m s^{-1} between 2 and 10 km. Clouds generated by the convection are rapidly elongated horizontally, so that

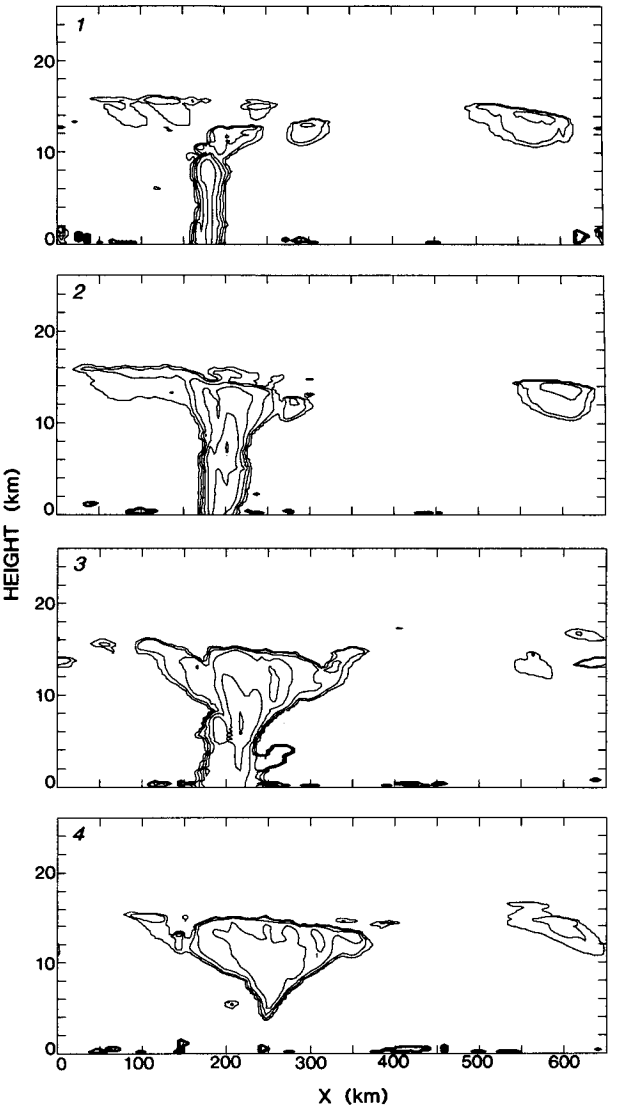

FIG. 1. Four snapshots of the mixing ratio for condensed water (cloud water plus rainwater plus snow), separated by 90 min. The contours are logarithmic. Successive contours differ by a factor of 10 in mixing ratio, the lowest contour corresponding to 10^{-7}.

classic anvil shapes are not often produced. The mean planetary albedo, the ratio of the reflected to the incident solar flux at the top of the model atmosphere, for the period shown in Fig. 3 is 37%, but there is considerable long-term variability. Partly because of the large shears produced and partly because of the long time scales in the radiative budget, which make it difficult to study, we forego a more detailed analysis of this integration and consider instead a model in which the mean winds are prescribed.

4. Localization

We next describe a model in which the mean winds are constrained to vanish identically. (The zonal mean

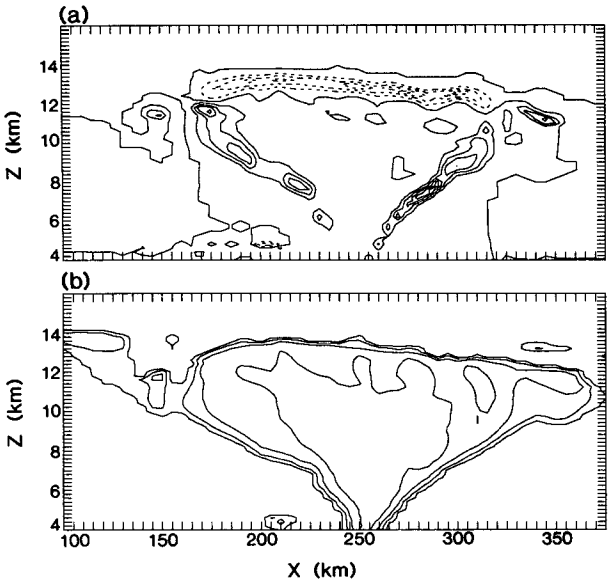

FIG. 2. (a) Radiative heating (5°C/day contour interval, with negative values stippled) and (b) mixing ratio for total condensed water (same contouring as in Fig. 1), for part of the domain in the last panel of Fig. 1.

of the horizontal wind is set to zero at each time step.) It was hoped that this would be the simplest way to generate homogeneous moist convective turbulence without the complication of the QBO-like oscillation.

Figure 4 shows the precipitation for a period of 3.6×10^6 s from this integration. The initial condition is the final state from the run shown in Fig. 3, but with the zonal mean winds removed. For the first 5×10^5 s, the convection is rather uniformly distributed in x. It then organizes slowly into two centers, dividing the domain nearly evenly. Within each of these centers the convection remains episodic. Finally, one of the centers emerges victorious, and deep convection thereafter occurs in only one spot.

Figure 5 shows the x-averaged net radiation (incoming minus outgoing) at the top of the model atmosphere during this integration, as well as the average relative humidity at 4 km. Starting from a value of ~ 50 W m^{-2}, the net radiation begins to decrease steadily, finally becoming negative. The trend in net radiation is primarily due to changes in planetary albedo, which increases from $\sim 30\%$ to nearly 50%, due to an increase in low-level cloud amounts in the stable, subsiding regions of the flow. The midtropospheric relative humidities also show a downward trend that is still continuing at the end of this integration.

The resulting strongly inhomogeneous heating distribution forces a large-scale circulation with low-level convergence in the convecting region. The time-mean flow over the last 4 days of the integration is shown in Fig. 6a. The convergence is very shallow, <600 m, and is partly balanced by outflow immediately above this layer and partly by outflow near the tropopause. The strength of the subsidence outside of the convecting region is such as to produce a transit time of ~ 40 days for air descending from the tropopause to the surface, consistent with the slow drying in Fig. 5.

By the end of the integration, there is a dramatic contrast between the moist convecting region and the very dry environment. Figures 6b and 6c show the vapor mixing ratio and the sum of the mixing ratios for cloud water, rainwater, and snow, averaged over the last 4 days of this integration. There is very little mixing of vapor between the wet convecting region and the dry subsiding region, and as a result there is a continuing drying of the latter as the very low mixing ratios near tropopause levels are advected downward. The upper-level clouds are homogeneously distributed, but at low levels the cloud amount increases steadily as the convective region is approached.

The deviation of the potential temperature from its zonal mean is shown in Fig. 6d. Near the surface, the air in the region of ascent is ~ 1°C warmer than the surface air elsewhere; between 1 and 6 km, it is colder by 1°–2°C. Adding the virtual temperature effect, the relative buoyancy of the air near the surface in the ascending region is enhanced by nearly a factor of 2. Aloft, the vapor mixing ratio approximately compensates for the cooler temperatures in the ascending air, and the horizontal differences in virtual potential temperature are a small fraction of 1°C.

We have performed an additional calculation in the same configuration, but with $T_s = 25$°C. The localization seems to take place more slowly in this case, and has a slightly different character. After an integration comparable in length to that in Fig. 4, the convection has become localized in one-half of the domain, but has not (yet?) become concentrated into one spot. The midtropospheric relative humidity still exhibits a downward trend, as does the net radiation at the top of the model, as in Fig. 5, but of weaker magnitude than in the warmer case.

Since the localization appears slowly, one suspects that it might be easily prevented. The flow near the surface is undoubtedly too quiescent at this resolution, and, as stated in the Introduction, additional noise in the boundary layer might be sufficient to maintain more homogeneous convective activity. This could be studied by increasing the resolution or adding some prescribed noise near the surface.

We have found an alternative method of avoiding this localization, by prescribing a nonzero zonal mean vertical shear. In particular, by fixing the zonal mean wind U (in m s^{-1}) to take the form

$$U = \begin{cases} 5z/h, & z < h = 5 \text{ km} \\ 5, & z > h, \end{cases} \tag{2}$$

the evolution of the precipitation shown in Fig. 7b results. The initial condition is the final state of the run

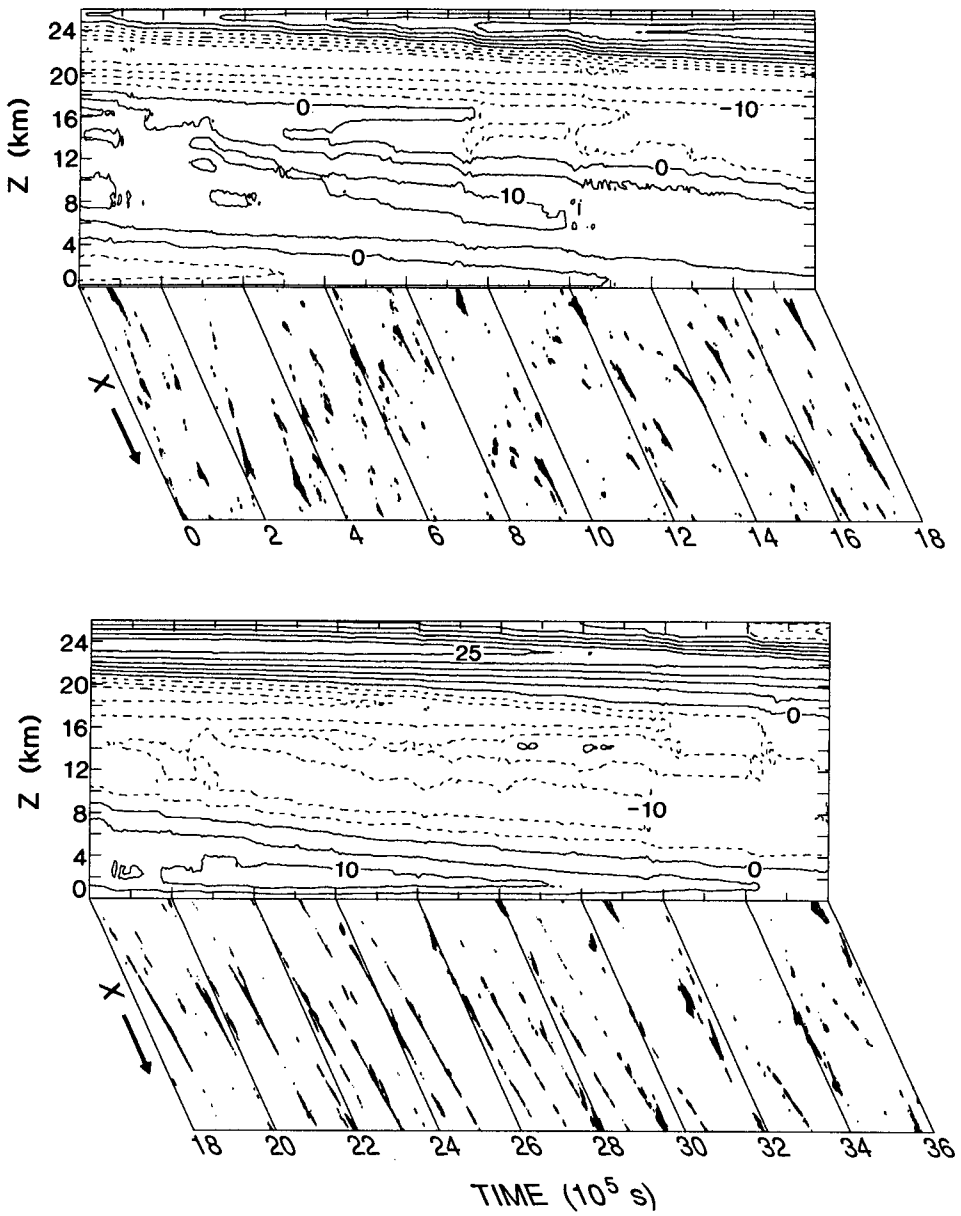

FIG. 3. Time evolution of precipitation at ground (as function of x) and domain-averaged zonal wind (as function of height). The contour interval for the wind is 5 m s^{-1}, with negative values stippled. A period of length 1.8×10^6 s is shown in the upper two panels, and the following period of the same length in the lower two.

shown in Fig. 4. (Approximately 10 days of the transition period have been omitted between Figs. 4 and 7b.) Additional short integrations suggest that an even smaller vertical shear would be sufficient to reestablish homogeneous convection.

In the experiments with prescribed shear, the "wet spot" appears to follow the bulk of the low- to midtropospheric moisture initially, as this moisture is advected by the prescribed mean winds, and then loses its coherence as the moisture is sheared out by this flow. Partly on the basis of these calculations, we are convinced that it is the moisture field, rather than the large-scale low-level convergence pattern, that gives the "wet spot" its memory. While alternative explanations are conceivable, involving resonant internal gravity waves, for example, we do not see how a small vertical shear, involving winds much smaller than gravity wave phase speeds, would then destroy the localization; neither is it clear how such an alternative explanation would account for

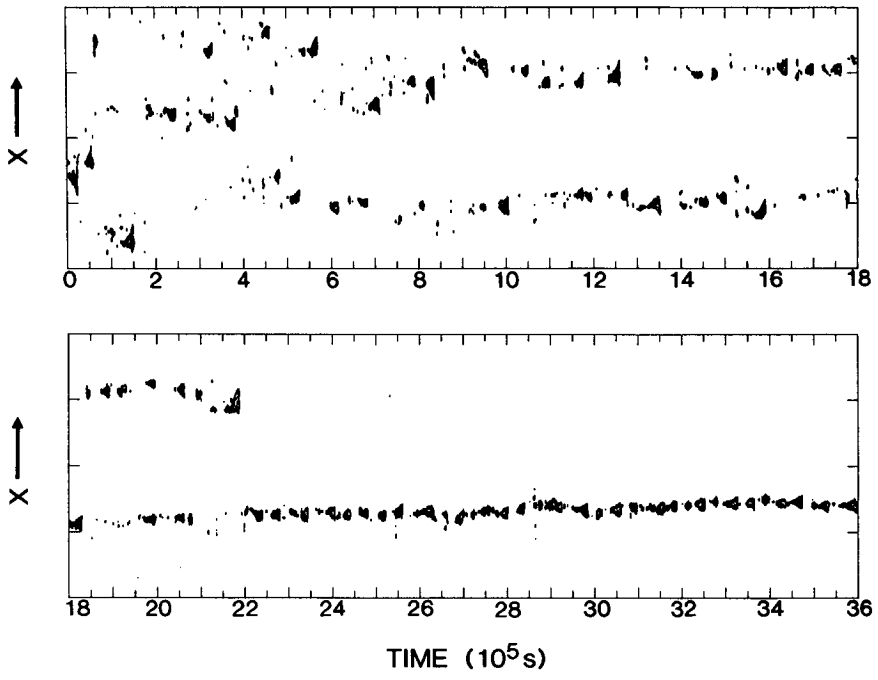

FIG. 4. Precipitation as a function of time and x in the case in which the mean wind is constrained to vanish.

essentially stationary, rather than propagating, wet spots.

5. An example of sensitivity to surface temperature

We describe two calculations, with $T_s = 30°$ and 25°C, using the model with the fixed vertical shear defined by (2). Time averaging is performed over 1.8×10^6 s in each case. The 30°C run was initialized from the "wet spot" final state of the case with no shear, with the first 10^6 s of the integration discarded. The case with 25°C was then initialized from the final state of this 30°C experiment, discarding $\sim 3 \times 10^6$ s in which the new equilibrium is approached.

A comparison between the precipitation patterns in these two integrations (Fig. 7) shows that propagation is more evident in the warmer run. However, this propagation does not have the flavor of a squall line. It appears to result from the advection of the low-level water vapor distribution, rather than the coherent movement of a zone of low-level convergence. The propagation speeds in Fig. 7b are only 1–2 m s^{-1}, typical of the imposed zonal flow in the moist layer near the surface.

To provide the reader with some feeling for the variability in the model, we show in Fig. 8 time series (without any time smoothing) of domain-averaged albedo, outgoing longwave flux, and 8-km relative humidity, from the 30°C case. Large variations in albedo and outgoing flux are to be expected for averages over this small domain, in which there is typically at most one deep convective event under way at a given time. In addition, there is substantial memory in the moisture field, which is subject to relatively weak restoring forces, as illustrated by the 7-day-long (6×10^5 s) trend toward moistening of the upper troposphere in the first half of this period. We have tried in the following to focus on those differences between the 25° and 30°C cases that are robust to changes in the averaging period.

Not all fields achieve approximate equilibrium after this length of integration. Figure 9 shows the x-averaged water vapor mixing ratio at 20 km from the 25°C experiment of Fig. 7a. Vapor is still mixing upward, presumably through the sporadic breaking of gravity waves and diffusion.

Figure 10 shows the mean temperature profiles in these two experiments, along with the adiabats computed assuming as the starting point a parcel with environmental moisture and temperature at 500 m. (The parcel ascends dry adiabatically until it becomes saturated near 1 km, and then follows the moist pseudo adiabat.) The temperature difference between the two model runs increases with height, reaching a maximum of 12.5 K at 12 km. (The difference in temperature between the two moist adiabats is 17 K at large heights.) The temperature at 16 km is larger by ~ 3 K in the case with warmer surface, but the energy balance here is subtle and could be dependent on the water vapor distribution, which is not in equilibrium above the tropopause.

It is evident that the tropopause is more or less at the location that would be predicted by a standard ra-

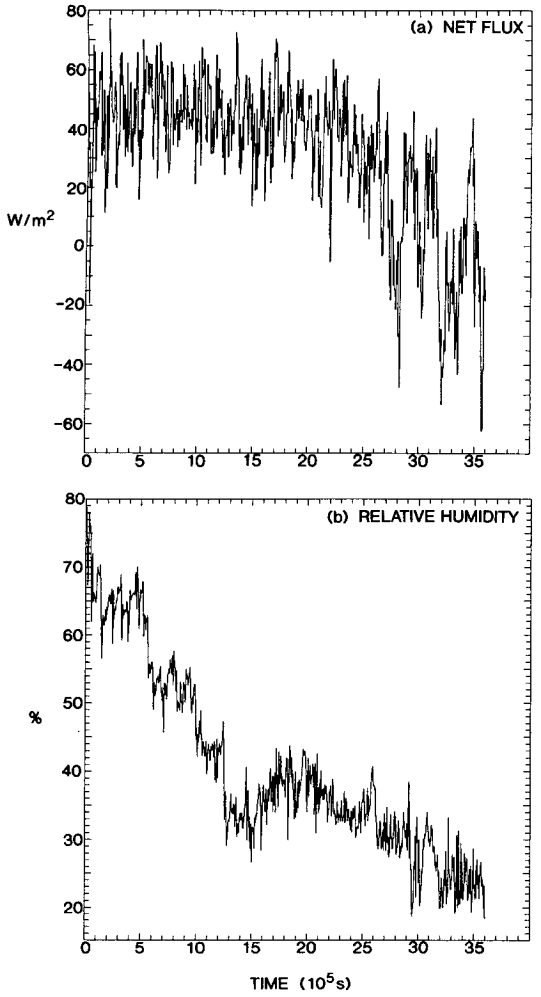

FIG. 5. Time evolution of domain-averaged (a) net radiative flux at the top of the atmosphere and (b) relative humidity at 4 km for the same time period as shown in Fig. 4.

diative–convective model with adjustment of temperatures to a moist adiabat (e.g., Lal and Ramanathan 1984). The departures from the moist-adiabatic profiles in Fig. 10 appear to be small; however, this difference is sensitive to the choice of the starting point for the adiabatic ascent. If one chooses the lowest model level, 100 m, the departures from the moist-adiabatic profiles are as large as 10 K in the upper troposphere of the warmer integration, and the associated value of CAPE is greater than 3000 $m^2\ s^{-2}$. The vertical velocities implied by this value of CAPE, >80 $m\ s^{-1}$ for undiluted ascent, bear little relation to the observed velocities in the cores, which rarely exceed 20 $m\ s^{-1}$, and are more typically ~10 $m\ s^{-1}$. The value of CAPE decreases rapidly as the starting level for the parcel is raised. This sensitivity of the CAPE to the choice of level is exaggerated by the large vertical gradient in the humidity profile near the surface. The values of CAPE for the 25°C case are typically 25% smaller than for 30°C, independent of the choice of starting level, as long as the same level is used in both cases.

The mean profiles of relative humidity are shown in Fig. 11a. Surface values are in excess of 90%. (These surface humidities are sensitive to the choice of a minimum wind speed in the expression for evaporation.) In the 25°C case, the relative humidity peaks at the lowest model level, while for 30°C, the peak is at the second level (300 m), a signature of the model's weak attempt to create a shallow mixed layer. An important

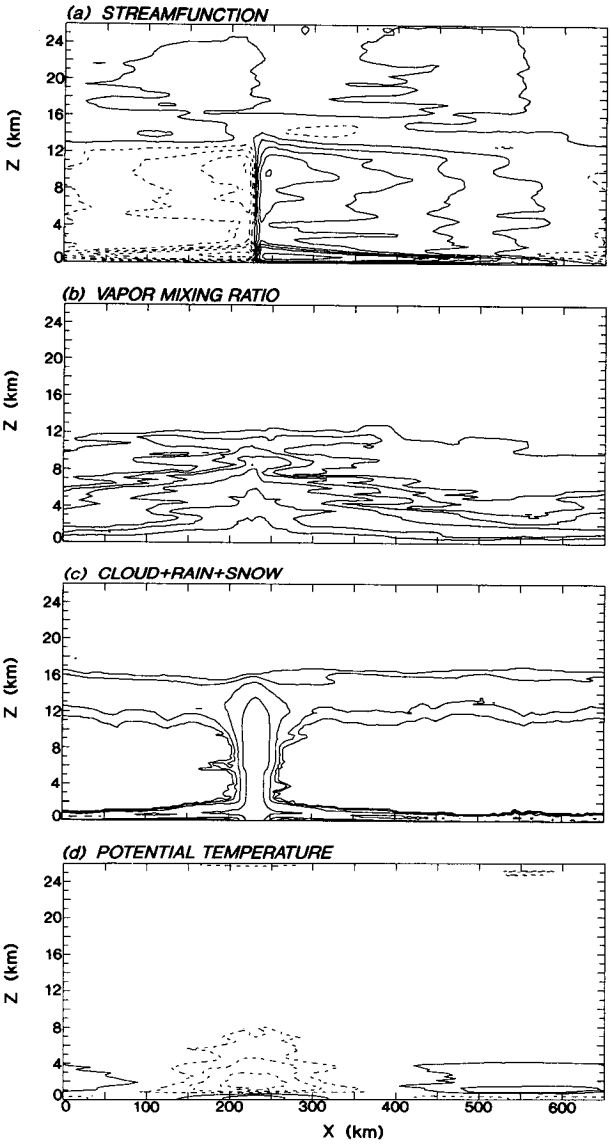

FIG. 6. Mean state averaged over last four days of the integration shown in Fig. 4. (a) Mass streamfunction: 2×10^2 kg $m^{-1}\ s^{-1}$ contour interval; maximum contour near the surface is 2×10^3; contours between 10^3 and 2×10^3 near the surface omitted. (b) Vapor mixing ratio: contours are (0.5, 1, 2, 4, 8, and 16) $\times 10^{-3}$. (c) Mixing ratio for condensed water: contours as in Fig. 1. (d) Deviation from x average of potential temperature: contour interval is 0.5 K, with negative contours stippled.

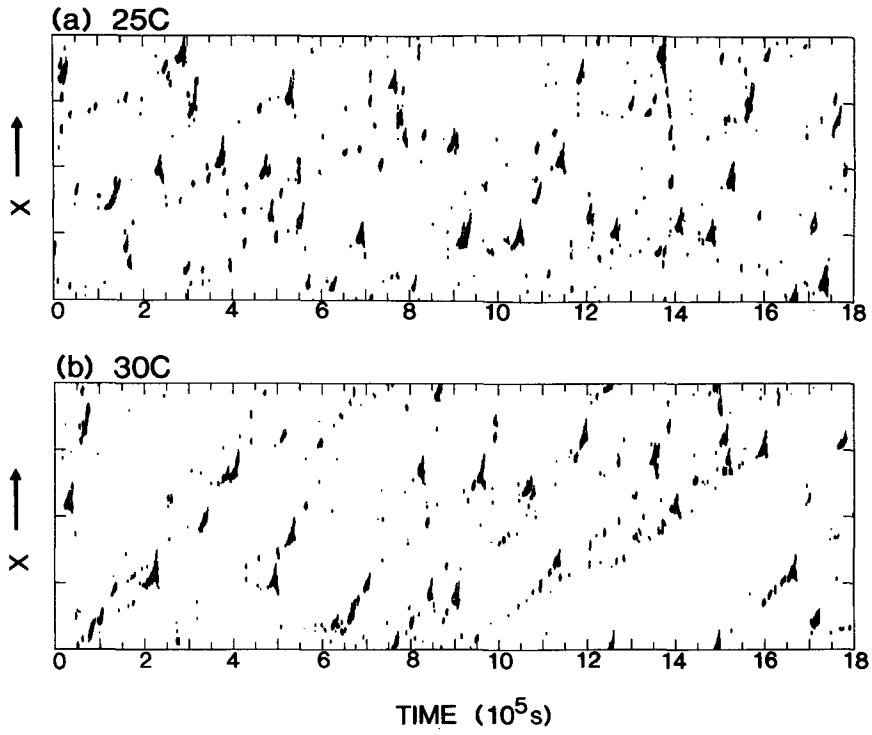

FIG. 7. Precipitation as a function of time and x in the case with a prescribed mean shear: (a) 25°C and (b) 30°C.

feature in these integrations is the upper-tropospheric maximum in relative humidity. Estimates of the climatological profiles averaged over the tropics typically decrease monotonically with increasing height (e.g., Manabe et al. 1965, Fig. 7.3). The model more closely resembles the profiles expected in actively convecting regions with heavy upper-level cloud cover.

The changes with increasing temperature are small in the lower troposphere. The upper-level maximum has shifted upward, and there is a decrease in relative humidity between 8 and 14 km. The *absolute* humidity increases everywhere in the troposphere.

The stratospheric changes are an artifact of the integration procedure. The final state of the 30°C case is the initial condition for the 25°C run, so the vapor has had a longer time in the latter case to "diffuse" upward.

The mixing ratios for cloud water and rainwater plus snow are displayed in Figs. 11b and 11c. There are two peaks in the cloud water. The low-level peak is reduced in strength by 25% in the warmer run, but occurs at the same height (700–900 m). The upper-level peak moves higher, from 10.5 to 12.5 km, retaining more or less the same magnitude. One sees an increase in rain at the ground and the raising of the rain/snow boundary with increasing temperature. Comparable amounts of water are contained in the cloud and rain/snow categories.

Figure 12 is a plot of the probability distribution for the total vertically integrated condensed water and for the low-level clouds alone (cloud water integrated from 0 to 2 km). The spike corresponding to cloud-free conditions is not shown. The water path in the low-level clouds typically lies between 10^{-2} and 10^{-1} kg m^{-2}, with the warmer case having somewhat smaller values on average. The probability of having no cloud water between 0 and 2 km is 69% in the 30°C case and 65% for 25°C. There are fewer, as well as thinner, low-level clouds in the warmer integration. (For the parameters used in our radiative model, unit optical depth in the visible is produced with integrated column condensed water content of $\sim 5 \times 10^{-3}$ kg m^{-2}.)

The solar heating and infrared cooling are shown in Fig. 13a. In the solar heating, one sees a low-level maximum greater than 1 K/day primarily associated with water vapor absorption, a maximum below the tropopause (near 13 km in the warmer case) of 0.5 K/day due to absorption by cloud water, and the ozone heating in the stratosphere. As the temperature increases, the heating increases throughout most of the troposphere, due to the increased vapor mixing ratios, and the peak associated with the upper-level clouds is elevated. Infrared cooling rates reach 3 K/day near the ground, with secondary maxima due to the upper-level clouds. The cooling increases with increasing temperature in the upper troposphere, except in the region

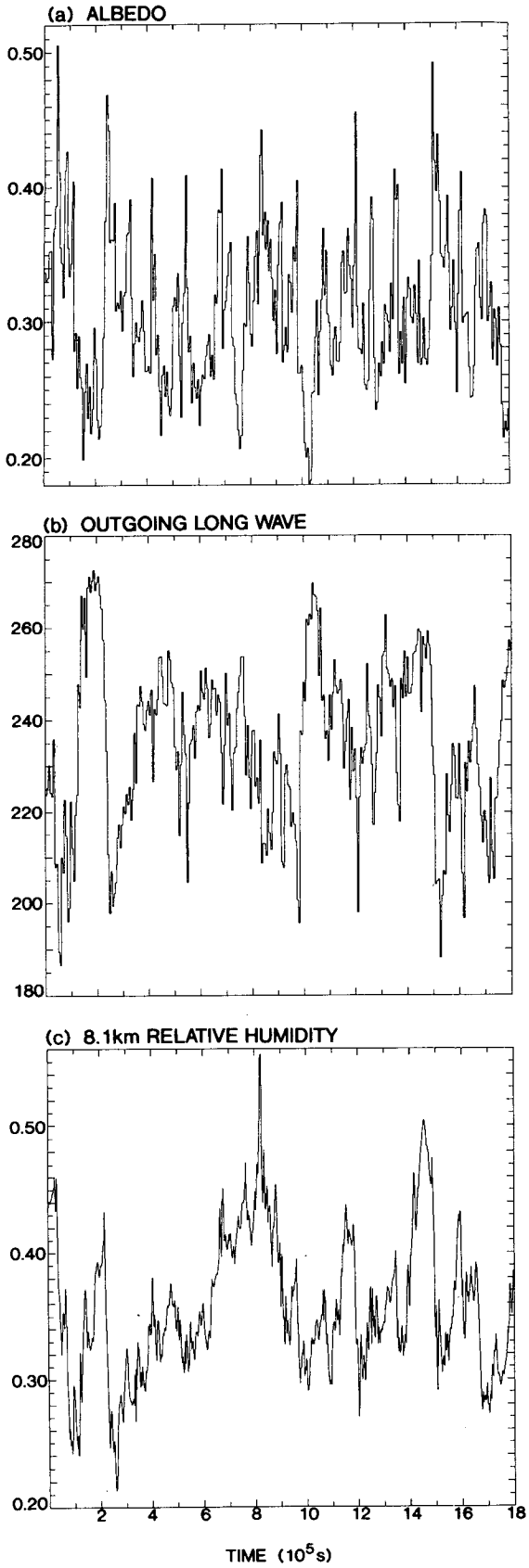

near 11 km that is affected by the elevation of the upper-level clouds.

The imbalance between the shortwave heating and longwave cooling is balanced by dynamic heating, and this residual is shown in Fig. 13b. There are three maxima in this profile. The upper maximum is associated with the destabilizing radiative heating/cooling created by the upper-level clouds, and shows that there are circulations associated with these clouds. The sharp minimum near 3 km is due to the maximum in solar heating and a weak minimum in the infrared cooling at this level. The entire pattern is displaced upward with increasing temperature, creating a substantial increase in dynamic heating throughout the upper troposphere (nearly 1 K/day at 10 km). The small residual dynamical heating in the stratosphere, maximizing in the sponge layer, appears to be a model artifact that we do not understand.

The energy balance at the top of the model atmosphere in these two experiments is shown in Fig. 14a. The outgoing longwave flux increases by ~ 14 W m^{-2} as T_* increases from 25° to 30°C. (We estimate the sampling error in the longwave flux to be 1–2 W m^{-2}.) A typical result for a radiative–convective model with fixed tropospheric lapse rate and fixed relative humidity is 2 W m^{-2} for each 1° increase in temperature. Somewhat larger values are produced by models that adjust to the moist adiabat (e.g., Lal and Ramanathan 1984), since this produces larger changes aloft for a given surface temperature change (an effect sometimes referred to as lapse rate feedback). Consistent with the result that the temperature change is similar to that predicted by a moist adiabat, and that the relative humidity changes and changes in *upper-level* cloudiness are small, the model's outgoing longwave flux responds in a similar way to that in conventional radiative–convective models.

The planetary albedo *decreases* from 0.34 to 0.30 as T_* increases from 25° to 30°C, a change that is attributable to the reduction in the *low-level* cloud cover and the water content of the clouds. (The estimated sampling error in each albedo is roughly 0.005.) The reduction in the reflected shortwave flux is comparable to the increase in the outgoing longwave flux. Therefore, the system is close to being neutrally stable. If the ocean temperature is perturbed, the change in the net flux of energy into the system is small, and the restoring force very weak. Since the response of the shortwave flux is dependent on the changes in low-level cloud water, and since the model does not form a well-defined boundary layer, we have little confidence in the robustness of this result.

FIG. 8. Time evolution of domain-averaged planetary albedo, outgoing longwave radiation, and relative humidity at 8 km for the 30°C case of Fig. 7.

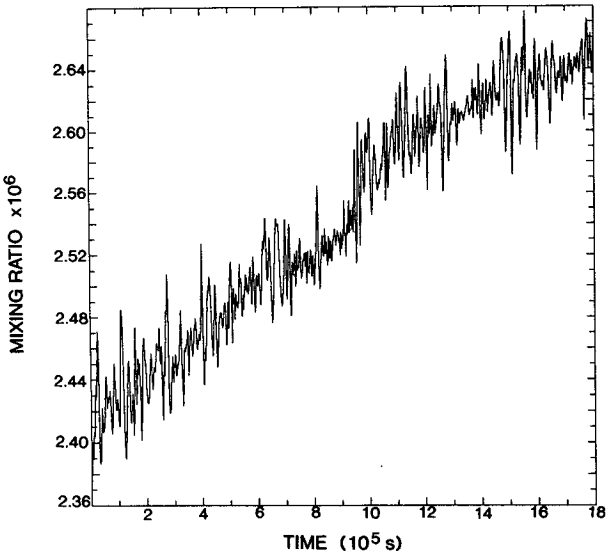

FIG. 9. Time evolution of mass mixing ratio of water vapor at 20 km, for the 25°C experiment, over the time interval shown in Fig. 7a.

The fluxes at the surface are shown in Fig. 14b. In equilibrium, the change in the flux into the ocean must be the same as the change at the top of the atmosphere—that is, near zero in this model. The increase in the downward longwave flux is greater than the increase in the upward flux (σT^4), a result that is also found in standard radiative–convective models in the tropics (the effective level of emission for the downward flux moves lower in the atmosphere, toward warmer temperatures, as the water vapor content increases). The evaporation (and, therefore, the precipitation) increases by more than 20%.

6. Comparison of the mean states with localized and homogeneous convection

Figure 15 compares the relative humidities and temperatures in the 30°C case (referred to as H for "homogeneous") with the profile obtained from the final 4 days of the experiment described in section 4 in which the convection has become localized (L). It should be kept in mind that L is not yet in equilibrium, the sense of the trend being such as to enhance the differences in Fig. 15. As expected, L is drier than H in the middle and lower troposphere. It is also warmer by ~4°–5°C throughout the atmosphere. An inversion develops in L below 1 km, below which the two temperature profiles are similar. (The two models have identical prescribed surface temperatures.) The tropopause is also sharper in L. The mean precipitation averaged over the domain is similar (within 10%) in the two cases.

The humidity difference is more easily understood. In L, the weakness of the horizontal mixing between the convecting and nonconvecting regions allows parcels to slowly descend from the upper to the lower troposphere with their upper-tropospheric mixing ratios nearly intact. In H, the integrity of the subsiding parcels is sporadically disrupted by convection.

The temperature differences are less easily explained. To first approximation, whether or not the environmental subsidence is interrupted by convection is of no importance to the potential temperature, since perturbations in potential temperature are redistributed horizontally through gravity waves. The upper-tropospheric moist static energy in L can only be matched to conditions in the lower troposphere if one assumes that parcels ascending in the cores become saturated at the lowest model level (100 m). Our interpretation is that the cores have their roots deeper in the boundary layer in L than in H, resulting in more moisture in the cores. These cores penetrate deeper, and the descent starts with larger potential temperature. It appears that the strength of the environmental subsidence is similar in the two cases (since the strengths of the two hydrologic cycles are similar), producing similar profiles except that L starts with a larger potential temperature near the tropopause. (This sensitivity of the temperature profile to convective organization could be dependent on the fact that the model does not support a well-defined well-mixed layer, which makes the precise level of the source of the air within the cores more important than it would otherwise be.) The warmer stratosphere is evidently a response to the increase in the upwelling longwave flux from the warmer troposphere.

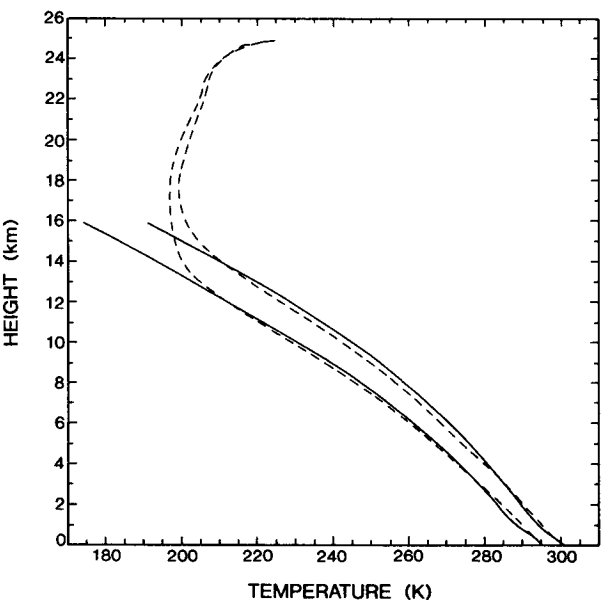

FIG. 10. Temperature as a function of height averaged over time and x, for 25° and 30°C cases (dashed lines). Adiabats computed as described in text are displayed by solid lines.

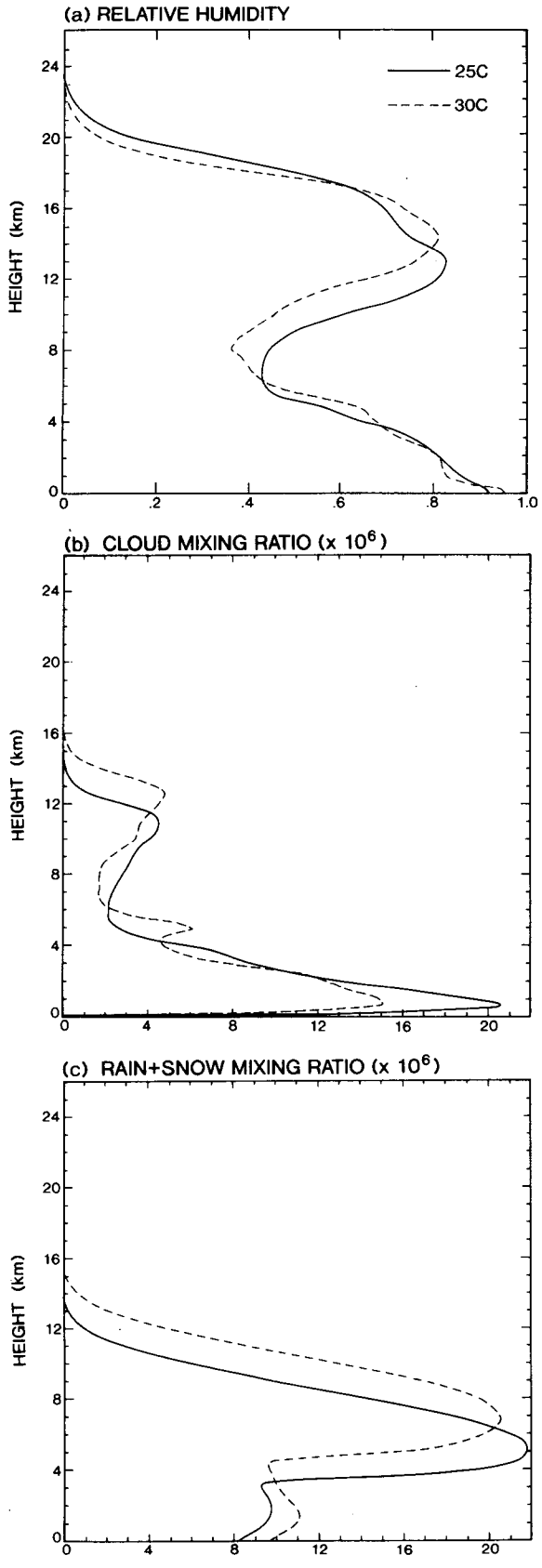

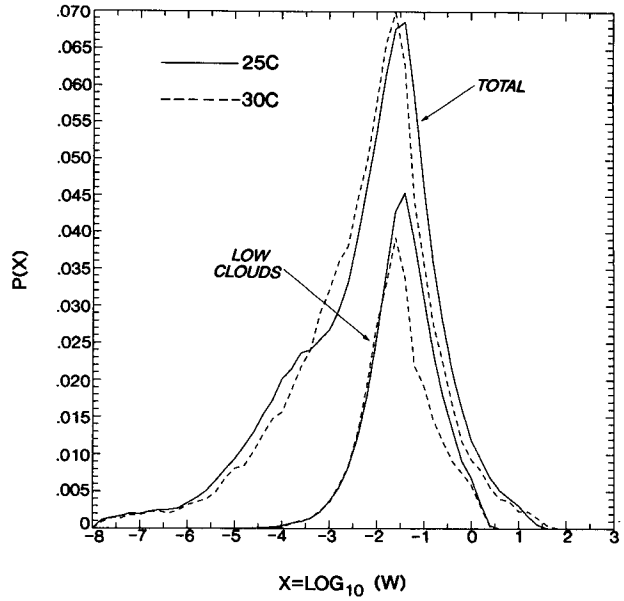

FIG. 12. Probability distribution for total column liquid + solid water, and for the contribution due to clouds below 2-km height. Solid lines (25°C); dashed lines (30°C). Horizontal axis is $\log_{10}(\text{kg m}^{-2})$.

7. Discussion and conclusions

The central importance of the complex of issues related to moist convection, clouds, and the hydrological cycle for studies of climate sensitivity has prompted us to attempt a calculation of radiative–convective equilibrium with explicit moist convection. We have chosen a relatively simple starting point—a two-dimensional domain (in x and z), periodic in x, with uniform prescribed surface temperature, and no rotation. While preliminary, these calculations have uncovered several potential complications. Two that have been highlighted here are 1) the generation of a QBO-like oscillation when the x-averaged winds are free to evolve, and 2) the localization of the convection when the x-averaged winds are constrained to vanish identically.

We hope to address basic questions about the QBO-like oscillation in future work. These include the explanations for the short period and the penetration into the troposphere. How does the period depend on the size of the domain? Is the descent in the troposphere gravity wave driven, as it presumably is in the model's stratosphere, or is it associated with convective eddy momentum fluxes? In the earth's tropics, the Hadley cell continually pumps low momentum air upward, thereby damping out any tendency of the observed QBO to penetrate to the tropopause (e.g., Saravanan

FIG. 11. (a) Relative humidity, (b) cloud mixing ratio, and (c) rain plus snow mixing ratio as a function of height averaged over time and x, for 25°C (solid lines) and 30°C (dotted lines).

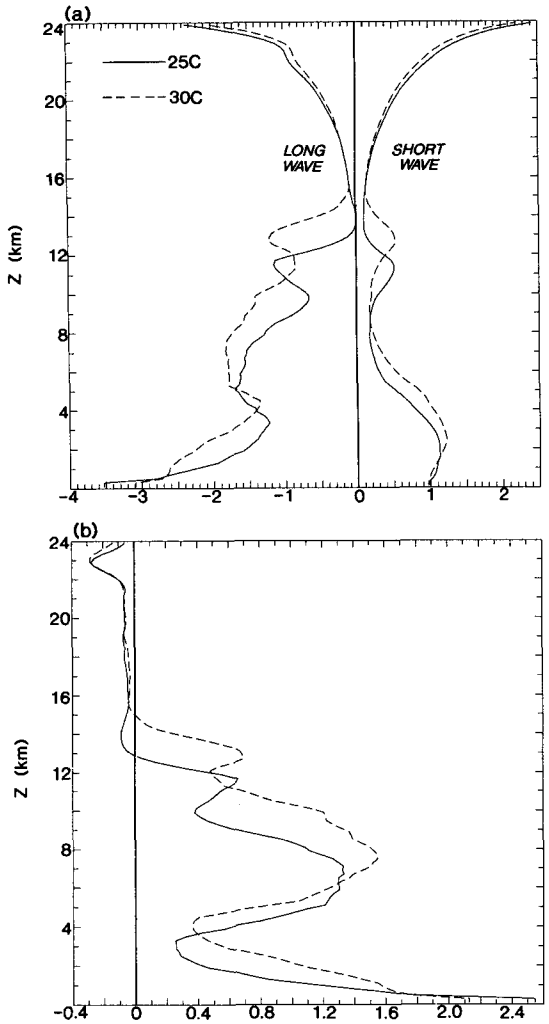

FIG. 13. (a) Solar heating and infrared cooling as a function of height, averaged over time and x, in degrees Celsius per day^{-1}; (b) the corresponding net dynamic heating.

QBO to penetrate to the tropopause (e.g., Saravanan 1990). In our 2D homogeneous model, no such transport mechanism exists.

The arbitrariness of the sponge layer could be of concern with regard to this "QBO" simulation, since the largest mean flows are observed within this layer. However, the WKB theoretical framework accepted as a good first approximation for the observed oscillation suggests that the behavior of the flow above some height z is irrelevant to the evolution of the oscillation at lower heights (Plumb 1977), implying that the details of the sponge are not important as long as substantial reflection does not occur.

The localization of the convection that occurs when the mean winds are set identically to zero appears to be a delicate process. A small amount of vertical shear in the wind is sufficient to destroy this localization. Also, the process proceeds much more slowly (if, indeed, it proceeds to completion) when the surface temperature is lowered. One can also speculate that stirring due to boundary-layer turbulence might be sufficient to maintain homogeneous convection in a more realistic model. However, the asymmetry is so profound by the end of the integration described in section 4 that we are skeptical that greater boundary-layer noise could kick the system out of this state. In some models it may be possible to obtain both homogeneously distributed and localized convective states for the same boundary conditions.

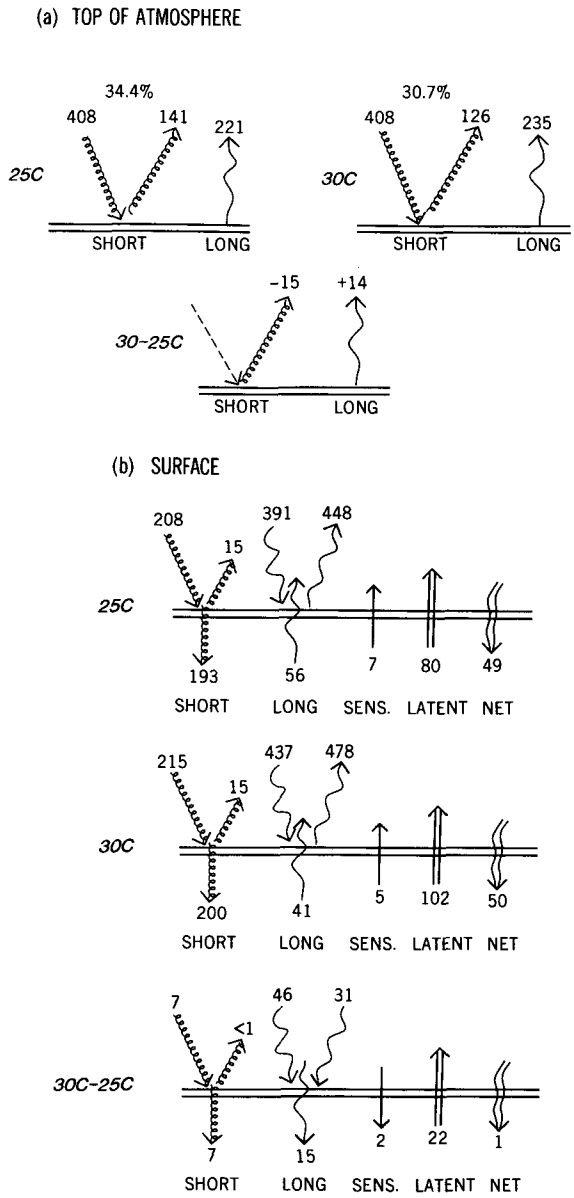

FIG. 14. (a) The time- and domain-averaged shortwave and longwave fluxes at the top of the atmosphere, in watts per square meter, for the 30° and 25°C cases, and the difference between these fluxes. (b) As in (a) but for the radiative and nonradiative energy fluxes at the surface.

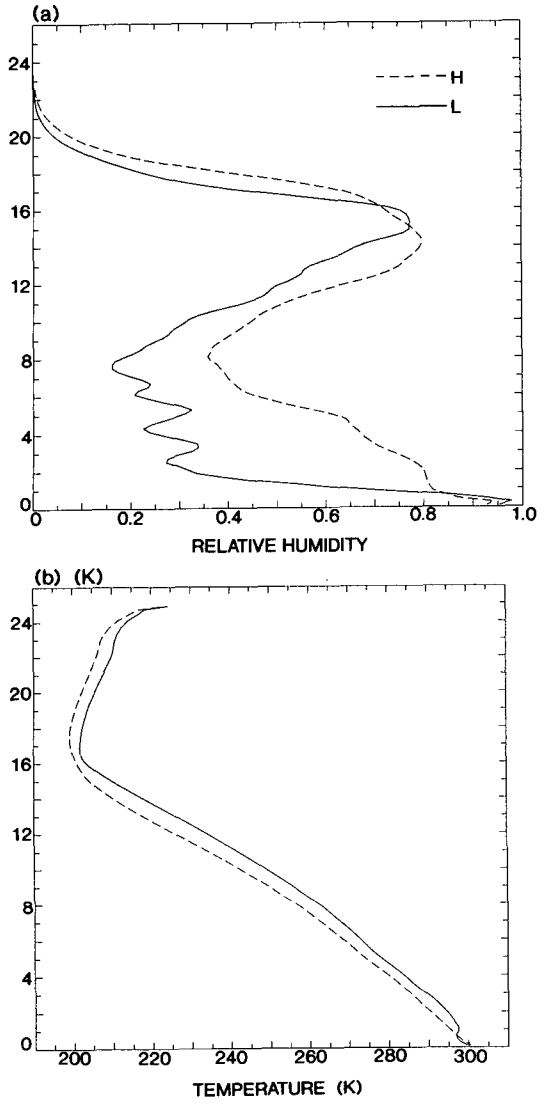

FIG. 15. Comparison of (a) relative humidity and (b) temperature profiles for experiments with localized convection (solid line, L) and homogeneous convection (dashed line, H).

It is intriguing that the system maintains two convecting centers for a substantial period before one of them succumbs. Perhaps a larger domain would be sufficient to stabilize the state with two centers. If this is the case, it would be interesting to explore the dependence of the number of these "wet spots" on the size of the domain and other model parameters.

The water vapor field evidently provides the memory for this localization, along with the low-level convergence that eventually is generated in the convecting region. Convection generates a moist atmosphere locally, and, in the absence of any mean shears, this moisture remains to encourage the convection to reform at the same location, long after the gravity wave activity excited by the convection has subsided. We presume that a key ingredient is the reduced entrainment of dry air into nascent plumes forming at low levels. Since much of this entrainment would be subgrid scale in the model, the localization could be sensitive to the subgrid-scale closure.

The choice of nonzero prescribed mean wind shear suppresses both of these "problems," and produces homogeneously distributed convection without the very long time scales associated with the model's "QBO." The resulting mean state is in many ways similar to the mean tropical atmosphere, although the relative humidity has a secondary maximum beneath the tropopause.

On increasing the surface temperature in this model, we find that the albedo decreases. The reduction in albedo is large enough to nearly balance the increase in the outgoing infrared flux, resulting in a model that would be close to a runaway condition, if surface temperatures were freed.

We do not place much confidence in this prediction of the behavior of the horizontally homogeneous system for several reasons. As pointed out in section 2, in the model's microphysics it is assumed that cloud water begins to convert into falling meteors immediately, if temperatures are sufficiently low to produce snow, while a critical cloud water concentration is required to begin the autoconversion of cloud to rain at higher temperatures. This difference in the treatment of rain and snow prevents upper-level cloud amounts from becoming excessive. The importance of the upper-level clouds for the model's response to surface temperature changes is likely sensitive to this assumption. Also, the accuracy of the radiative transfer is limited by several assumptions: there is no discrimination between the various hydrometeors; all particles are assumed to be spheres and to have the same size; and the heating rates are updated rather infrequently, possibly distorting the cloud–radiation interactions. Furthermore, there is no explicit boundary-layer parameterization in the model, beyond the subgrid-scale mixing formulation, and a well-defined mixed layer is not generated. Therefore, the low-level clouds predicted by the model, which are responsible for most of the albedo change, must be treated skeptically. Finally, a preliminary comparison of 30°C and 25°C cases of the "QBO" model with unconstrained mean winds shows the opposite tendency—albedos increasing with increasing temperature.

The fact that the convection localizes spontaneously when the zonal mean flow is constrained to be zero provides the opportunity of studying the effects of the convective organization on the mean atmospheric temperature profile. Midtropospheric relative humidities are much lower in the case with localized convection, and temperatures are warmer (by more than 5°C) above the model's trade wind inversion. This result would be greatly altered in a model with predicted surface temperature, since albedos are much higher when

convection is localized, due to enhanced low-level cloudiness. It is nevertheless of interest that temperatures throughout most of the troposphere can be altered in this model by more than 5°C, with fixed surface temperature.

The list of calculations needed to clarify and solidify these preliminary results is a long one. In the context of the homogeneous 2D model, one should test the sensitivity to horizontal resolution and to the subgrid-scale mixing formulation, especially as it affects mixing in the boundary layer and low-level cloudiness. The dependence on the "gustiness factor"—the imposed minimum wind speed in the surface flux formulation—should also be examined. (Is the strength of the hydrologic cycle sensitive to this choice, or would the relative humidity adjust to maintain a similar mean evaporation rate?) The possible importance of unresolved boundary-layer turbulence for initiating convection should be considered. Differences in the radiative properties of various types of hydrometeors are undoubtedly important, and should be incorporated in the model. Likewise, the dependence of cloudiness on the microphysical model, and on the microphysics–radiation interactions, is also likely to be important. Would any of these changes in the model alter the QBO-like oscillation significantly, or the localization of convection into "wet spots" when there are no mean winds?

It will also be of interest to examine lower-resolution hydrostatic models with embedded convective parameterizations and cloud prediction schemes, in exactly the same two-dimensional periodic framework. Would such models produce a "QBO" or the convective localization? Would they have the same sensitivity to changes in surface temperature?

Comparable three-dimensional calculations are a very natural problem for the next generation of parallel machines. An interesting transitional calculation may be a $2\frac{1}{2}$-dimensional model in an anisotropic domain, in which there are only enough grid points in the third dimension to allow the individual cores to develop a 3D structure. Both rotation and inhomogeneous forcing can be introduced in the 2D framework, but 3D calculations with these added complications will be needed for quantitative studies relevant for climatic sensitivity.

Acknowledgments. This work would not have been possible without Frank Lipps's cloud modeling effort at GFDL over many years. Due to his untimely death in 1990, just as we were beginning to plan these calculations, we have had to proceed as best we could without his guidance. We dedicate this work to his memory. We also thank Leo Donner and Steve Garner for many helpful comments.

APPENDIX A

The Convective Cloud Model

The three-dimensional counterpart of the convective cloud model used in this study has been previously described in detail in Lipps and Hemler (1982, 1986, 1991) and Hemler et al. (1991)—hereafter LH82, LH86, LH91, and HLR. In this Appendix we discuss new features of the model that have not been previously presented.

a. The elastic equations

An elastic version of the model is used in this study, with the simplest form of a prognostic pressure equation, similar to that in Klemp and Wilhelmson (1978), in which the change in the perturbation Exner function Π_1 results solely from the local divergence field:

$$\frac{\partial \pi_1}{\partial t} + \frac{c^2}{c_p \theta_0 \rho_0}\left(\frac{\partial \rho_0 u}{\partial x} + \frac{\partial \rho_0 w}{\partial z}\right) = 0. \qquad \text{(A1)}$$

Here $\Pi_1 = (p_1/p_0)^{R/c_p}$, where p_1 is the perturbation pressure and p_0 is 1000 mb. The perturbation pressure is defined as the departure of the pressure from the horizontal mean state. The remaining quantities in (A1) are the specific heat at constant pressure (c_p), the basic-state potential temperature ($\theta_0(z)$), density ($\rho_0(z)$), and speed of sound ($c^2(z)$), and the velocity components (u and w). Comparisons between cloud simulations using (A1) and the complete prognostic pressure equation have suggested that these differences have little effect on the convection, so we have chosen the simplified form for this preliminary study.

The terms responsible for vertically propagating sound waves in the vertical velocity and pressure equations are solved implicitly in the vertical, following the scheme discussed in Durran and Klemp (1983). Unlike that study, however, we do not need a smaller time step to integrate the acoustic components of the equations, because of the relatively large Δx and small Δz used here.

Since nondivergence is not imposed in this elastic model, the advection scheme used in previous versions of this model is replaced by scheme c_3 of Piacsek and Williams (1970), formed by averaging the flux and advective forms, which absolutely conserves second-order quantities.

b. The cloud physics parameterization

The model employs a simplified bulk cloud physics, which includes water vapor (q_v), cloud water/ice (q_c), rainwater (q_r), and ice/snow (q_s). The prognostic ice variable and cloud ice parameterization are new additions to the previously existing scheme, documented most recently in HLR. The prognostic ice/snow variable q_s has an assumed density (0.1 g cm^{-3}) and relative fall velocity appropriate for snow, and is designed for investigation of anvil ice processes rather than hail or heavy graupel formation where the interaction of ice and rainwater is significant. Changes have been made in some of the warm-rain cloud physics so that it is

consistent with the expressions used in the snow parameterization.

The cloud mixing ratio (q_c), which represents both cloud water and cloud ice, increases when the vapor in supersaturated air condenses and is reduced to zero when the air becomes subsaturated. At temperatures warmer than T_0 (−6°C), only cloud water (q_{cw}) is assumed to be present, the latent heat of vaporization is released at condensation, and supersaturation is determined with respect to liquid, while at temperatures below T_{00} (−12°C), q_c is assumed to be all cloud ice (q_{ci}), the latent heat of sublimation is released at condensation, and supersaturation is determined with respect to ice. At intermediate temperatures a mixture of cloud water and cloud ice is assumed present, with the percentage of each form varying linearly with temperature. The latent heat and saturation mixing ratio are also calculated as a weighted mean of the values relevant for liquid and ice processes, following the treatment of Lord et al. (1984).

The prognostic equations for water vapor, cloud water/ice, rainwater, and snow are

$$\frac{\partial \rho_0 q_v}{\partial t} = \text{ADV} + \text{DIFF} - \rho_0(\text{COND} + \text{EVAP} + \text{DEPO}) \quad \text{(A2)}$$

$$\frac{\partial \rho_0 q_c}{\partial t} = \text{ADV} + \text{DIFF} + \rho_0(\text{COND} - S_{ar} - S_{as} - S_{cr} - S_{cs}) \quad \text{(A3)}$$

$$\frac{\partial \rho_0 q_r}{\partial t} = \text{ADV} + \text{DIFF} + \frac{\partial \rho_0 V_r q_r}{\partial z} + \rho_0(S_{ar} + S_{cr} + \text{EVAP} + \text{MELT}) \quad \text{(A4)}$$

$$\frac{\partial \rho_0 q_s}{\partial t} = \text{ADV} + \text{DIFF} + \frac{\partial \rho_0 V_s q_s}{\partial z} + \rho_0(S_{as} + S_{cs} + \text{DEPO} - \text{MELT}), \quad \text{(A5)}$$

where ADV are the advection terms, DIFF the diffusion terms, and COND the condensation/evaporation of the cloud water/ice. The representation of these terms is discussed in LH82 and LH86. The remaining terms represent transformations of water from one form to another and are defined below. The transformations involving rain and snow follow those used by Lin et al. (1983). Note that rain–snow and rain–cloud ice processes other than melting of snow are not included in the model.

The relative fall velocities of snow and rain (in m s^{-1}) are given by

$$V_s = 1.192(10^3 \rho_0 q_s)^{0.0625}(\rho_{00}/\rho_0)^{0.5} \quad \text{(A6)}$$

$$V_r = 5.23(10^3 \rho_0 q_r)^{0.2}(\rho_{00}/\rho_0)^{0.5} \quad \text{(A7)}$$

where ρ_{00} is a reference density of 1.20416 kg m^{-3}.

Autoconversion is the mechanism by which rainwater and snow are initially created. The autoconversions of cloud ice to snow (S_{as}) and cloud water to rain (S_{ar}) are modeled by

$$S_{as} = 10^{-3} e^{0.025T}(q_{ci} - q_{ci,cr}) \quad \text{(A8)}$$

$$S_{ar} = 10^{-3}(q_{cw} - q_{cw,cr}) \quad \text{(A9)}$$

where the critical mixing ratios required for autoconversion are set as $q_{ci,cr} = 0$ and $q_{cw,cr} = 1.5$ g kg^{-1}. The rationale for the former choice is discussed in section 2.

Accretion or collection is the process by which falling rain and snow collect cloud water or cloud ice that is encountered. Expressions for S_{cs} (collection by snow) and S_{cr} (collection by rain) are given by

$$S_{cs} = 1.484(\rho_0 q_s)^{0.8125}(\rho_{00}/\rho_0)^{0.5} q_c G(T) \quad \text{(A10)}$$

where

$$G(T) = \begin{cases} 1 & \text{for } T \geq -6°\text{C} \\ (T + 12)/6 - [(6 + T)/6]e^{0.025T} & \text{for } -12°\text{C} \leq T \leq -6°\text{C} \\ e^{0.025T} & \text{for } T \leq -12°\text{C}, \end{cases}$$

and

$$S_{cr} = 3.272(\rho_0 q_r)^{0.95}(\rho_{00}/\rho_0)^{0.5} q_c. \quad \text{(A11)}$$

Transfer of water substance between snow and vapor may go in either direction depending on the environmental relative humidity. Sublimation of snow, and deposition from vapor to snow, occur when snow is present in an environment subsaturated and supersaturated with respect to ice, respectively. The expression for both of these processes is given by

$$\text{DEPO} = -(q_{si} - q_v)[7.495 \times 10^{-3}(\rho_0 q_s)^{0.5} + 6.771 \times 10^{-2}(\rho_0 q_s)^{0.65625}(\rho_{00}/\rho_0)^{0.25}] \quad \text{(A12)}$$

where the sign of $(q_{si} - q_v)$ determines whether deposition or sublimation occurs. Analogously, the evaporation of rain is given by

$$\text{EVAP} = -(q_{sw} - q_v)[3.870 \times 10^{-3}(\rho_0 q_r)^{0.5} + 6.678 \times 10^{-2}(\rho_0 q_r)^{0.725}(\rho_{00}/\rho_0)^{0.25}]. \quad \text{(A13)}$$

The expression for snowmelt is

$$\text{MELT} = 6.14 \times 10^{-2} \times \{7.164 \times 10^{-4}(T - T_f)\rho_0^{-1} - 2.739(q_{wsf} - q_v)\} \times \{(\rho_0 q_s)^{0.5} + 5.894(\rho_0 q_s)^{0.65625}(\rho_{00}/\rho_0)^{0.25}\} + 1.259 \times 10^{-2}(T - T_f)S_{cs}, \quad \text{(A14)}$$

where q_{wsf} is the saturation mixing ratio at the freezing point T_f. Melt occurs only when $T > T_f$ and is significantly reduced in very dry environments ($q_{wsf} - q_v$ large). The last term represents the melting associated

with collection by the snow of cloud water at temperatures above freezing.

c. *Variation of the thermodynamic base state with time*

As discussed in the scale analysis of LH82, this convective model was developed with the assumption that the thermodynamic variables can be represented as the combination of a zero-order base state that is a function of height only and a first-order component, varying in space and time, that is an order of magnitude smaller: $\theta = \theta_0(z) + \theta_1(x, z, t)$. Such a representation is valid for use in cloud modeling studies in which the time elapsed is typically only a few hours. However, for longer integrations, θ_1 can become large in response to continuing large-scale forcing, causing the model's formulation of both the dynamics and the condensation process to lose accuracy with time.

To avoid this problem, we have introduced a time-varying base state. On each time step, θ_0 and all other thermodynamic base-state variables are redefined so that the horizontal average of θ_1 equals zero. In this way, θ_1/θ_0 remains small, and the model assumptions are not violated. In tests with short integrations, it was found to be preferable to update the base state every time step to avoid slight discontinuities in the evolution, although the sensitivity to the updating period was very small. While this procedure does destroy the exact energy conservation properties of the model, it does not appear to cause a significant spurious energy source. A more general formulation of the model that does not require this linearization and updating procedure would be preferable, and should be straightforward in this elastic framework.

APPENDIX B

Radiative Transfer Model

The solar and longwave radiative transfer schemes employed in this study are described below.

a. *Solar*

We adopt a formulation that combines the delta–Eddington method with an adding scheme similar to that in Coakley et al. (1983). The solar spectrum is divided into 56 intervals; the central wavelength and the bandwidth of each interval are listed in Table 1.

The constituents and their respective optical properties over the 56 spectral intervals are similar to those considered by Ramaswamy and Kiehl (1985, hereafter RK), with the following exceptions: aerosols are not included here; a new prescription is adopted for cloud optical properties; and the solar spectral irradiance follows Labs and Neckel (1970).

First, the single scattering properties (extinction optical depth τ_{ext}, single scattering albedo ω, and the asymmetry factor g) are evaluated for each spectral interval and in each layer. For both water and ice clouds, the single scattering properties are represented in terms of water path and effective radius following Slingo (1989). In this exploratory study, the effective radius is assumed to be 5 μm. We recognize that this is an arbitrary assumption that is probably justifiable only for the low-lying water clouds. We hope to examine the sensitivity to the condensate sizes and types in future experiments. The condensed water path is determined prognostically in each layer by the microphysical and advective processes in the cloud model.

TABLE 1. The central wavelength and the bandwidth of each interval used in the calculation of the solar fluxes. The centers of the first 45 bands are separated by 0.01 μm. The last band accounts for all solar insolation greater than 3.7 μm.

Interval	Band center (μm)	Bandwidth (μm)
1–45	0.21 (0.01) 0.65	0.01
46	0.66	0.05
47	0.74	0.084
48	0.83	0.096
49	0.95	0.121
50	1.11	0.269
51	1.43	0.298
52	1.62	0.095
53	1.89	0.529
54	2.60	0.791
55	3.30	0.610
56	11.00	—

Next, the reflection and transmission characteristics of each layer in each spectral interval are obtained using the delta–Eddington approximation (Coakley et al. 1983). These functions depend on the single scattering properties of the layers (RK). If a layer contains a number of constituents, each of which interacts with the solar spectral frequency under consideration, the layer single scattering properties are prescribed as follows:

$$\tau_{ext}(\text{layer}) = \sum_i \tau_{ext,i} \tag{B1}$$

$$\omega(\text{layer}) = \sum_i \tau_{scat,i} / \sum \tau_{ext,i} \tag{B2}$$

$$g(\text{layer}) = \sum_i \tau_{scat,i} g_i / \sum \tau_{scat,i} \tag{B3}$$

where the sums are over all the constituents present in that layer.

The up and down fluxes at the various levels can be formulated in terms of the reflection and transmission characteristics of the layers, taking care to distinguish between the properties appropriate for the direct (unscattered) and diffuse beams. (The importance of the latter distinction is pointed out by Coakley et al. 1983.) This technique differs from that employed by RK. With level 1 at the top of the model, the following relations are obtained for the fluxes:

$$S_1^{\downarrow} = S_{1d}^{\downarrow} = S_0 \tag{B4}$$

$$S_1^{\uparrow} = S_{1d}^{\downarrow} R_1^d + S_2^{\uparrow} T_1^f \tag{B5}$$

$$S_2^{\downarrow} = S_{1d}^{\downarrow} t_1^d + S_{1d}^{\downarrow} t_1^f + S_2^{\uparrow} R_1^f = S_{2d}^{\downarrow} + S_{2f}^{\downarrow} \tag{B6}$$

$$S_2^{\uparrow} = S_{1d}^{\downarrow} t_1^d R_2^d + S_{2f}^{\downarrow} R_2^f + S_3^{\uparrow} T_2^f \tag{B7}$$

$$S_3^{\downarrow} = S_{1d}^{\downarrow} t_1^d t_2^d + S_{1d}^{\downarrow} t_1^d t_2^f + S_{2f}^{\downarrow} T_2^f + S_3^{\uparrow} R_2^f = S_{3d}^{\downarrow} + S_{3f}^{\downarrow} \tag{B8}$$

$$S_{i-1}^{\downarrow} = S_{i-1,d}^{\downarrow} + S_{i-1,f}^{\downarrow} \tag{B9}$$

$$S_i^{\downarrow} = S_{i,d}^{\downarrow} + S_{i,f}^{\downarrow} \tag{B10}$$

$$S_i^{\uparrow} = S_{1d}^{\downarrow} \left(\prod_{k=1}^{i-1} t_k^d \right) R_i^d + S_{i,f}^{\downarrow} R_i^f + S_{i+1}^{\uparrow} T_i^f ; \tag{B11}$$

S_0 is the solar spectral irradiance at the top. Further,

$$t_i^d = \exp\left(-\frac{\tau_i}{\mu_0} \right) \tag{B12}$$

$$S_{i,d}^{\downarrow} = S_{1d}^{\downarrow} \left(\prod_{k=1}^{i-1} t_k^d \right) \tag{B13}$$

$$S_{i,f}^{\downarrow} = S_{i-1,d}^{\downarrow} t_{i-1}^f + S_{i-1}^{\downarrow} T_{i-1}^f + S_i^{\uparrow} R_{i-1}^f \tag{B14}$$

with $S_{i,f}^{\downarrow} = 0$ and

$$t_i^f = T_i^d - \exp\left(-\frac{\tau_i}{\mu_0} \right) = T_i^d - t_i^d ; \tag{B15}$$

T_i^d denotes the total (direct plus diffuse) transmissivity of the direct incident radiation through layer i while t_i^d and t_i^f denote, respectively, the direct and diffuse components of T_i^d; μ_0 is the cosine of the incident solar zenith angle. The transmissivity of diffuse incident radiation by layer i is denoted by T_i^f. The reflection functions of the layers are represented by R, with the superscripts denoting whether they are with respect to direct (d) or diffuse (f) beams incident on the layer. Similarly, the subscripts d and f on the down ($S^{\downarrow}$) fluxes indicate whether they represent the direct or diffuse beam. The upward flux ($S^{\uparrow}$) is always diffuse. Direct radiation once scattered is assumed to be diffuse, and the diffuse beam is assumed to be isotropic.

The equations (B4)–(B11) are rearranged in the form of a pentadiagonal matrix that is then inverted to obtain the up and down fluxes. This procedure is repeated for each of the 56 spectral intervals.

b. Longwave

The longwave transfer scheme is similar to that in RK. The gases considered are H_2O, CO_2, O_3, CH_4, N_2O, and CFCs. Current concentrations are employed. In the infrared, clouds are assumed to be absorbers only; their scattering properties are ignored. Further, their absorption is assumed to be "gray" in the longwave spectrum.

The treatment of the overlap in the longwave between cloud water and each gas follows the same prescription as that for aerosols in RK, wherein the absorptance due to a gas–cloud combination is written as

$$A_{\text{TOTAL}} = \int (1 - T_\nu^{\text{gas}} T_\nu^{\text{cloud}}) d\nu \tag{B16}$$

$$T_\nu^{\text{cloud}} = \exp(-1.66 \alpha W) \tag{B17}$$

where the integral in (B16) is over frequency and T^{gas} and T^{cloud} denote the transmission of diffuse radiation through gas and cloud.

The absorption coefficient α is assumed to be 0.1 $\text{m}^2\ \text{gm}^{-1}$; this value is a fair, but not necessarily very accurate, choice for representing the water and ice phases (Stephens 1978; Chylek and Ramaswamy 1981; Stephens and Webster 1981). In (B17), the diffusivity factor has been assumed to be 1.66, and W denotes the total hydrometeor (water plus ice) path in each layer.

REFERENCES

Betts, A. K., and W. Ridgeway, 1989: Climatic equilibrium of the atmospheric convective boundary layer over the tropical ocean. *J. Atmos. Sci.*, **46,** 2621–2641.

Chylek, P., and V. Ramaswamy, 1982: Simple approximation for infrared emissivity of water clouds. *J. Atmos. Sci.*, **39,** 171–177.

Coakley, J. A., R. D. Cess, and F. B. Yurevich, 1983: The effect of tropospheric aerosol on the Earth's radiation budget: A parameterization for climate models. *J. Atmos. Sci.*, **40,** 116–138.

Durran, D. R., and J. B. Klemp, 1983: A compressible model for the simulation of moist mountain waves. *Mon. Wea. Rev.*, **111,** 2341–2361.

Emanuel, K. A., 1987: An air–sea interaction model of intraseasonal oscillations in the tropics. *J. Atmos. Sci.*, **44,** 2324–2340.

Gregory, D., and M. J. Miller, 1989: A numerical study of the parameterization of deep tropical convection. *Quart. J. Roy. Meteor. Soc.*, **115,** 1209–1241.

Hemler, R. S., F. B. Lipps, and B. B. Ross, 1991: A simulation of a squall line using a nonhydrostatic cloud model with a 5-km horizontal grid. *Mon. Wea. Rev.*, **119,** 3012–3033.

Holton, J. R., and R. S. Lindzen, 1972: An updated theory of the quasi-biennial oscillation of the tropical stratosphere. *J. Atmos. Sci.*, **29,** 1076–1080.

Islam, S., R. L. Bras, and K. Emanuel, 1993: Predictability of mesoscale rainfall in the tropics. *J. Appl. Meteor.*, **32,** 297–310.

Joseph, J. H., W. Wiscombe, and J. A. Weinman, 1976: The delta–Eddington approximation for radiative transfer. *J. Atmos. Sci.*, **33,** 2452–2459.

Kessler, E., 1969: *On the Distribution and Continuity of Water Substance in Atmospheric Circulations.* Meteor. Monogr., No. 32, Amer. Meteor. Soc., 84 pp.

Klemp, J. B., and R. B. Wilhelmson, 1978: The simulation of three-dimensional convective storm dynamics. *J. Atmos. Sci.*, **35,** 1070–1096.

Labs, D., and H. Neckel, 1970: Transformation of the absolute solar radiation data into the international temperature scale. *Solar Phys.*, **15,** 79–87.

Lal, M., and V. Ramanathan, 1984: The effect of moist convection and water vapor radiative processes on climatic sensitivity. *J. Atmos. Sci.*, **41,** 2238–2249.

Lin, Y.-L., R. D. Farley, and H. D. Orville, 1983: Bulk parameterization of the snow field in a cloud model. *J. Climate. Appl. Meteor.*, **22,** 1065–1092.

Lindzen, R. S., and J. R. Holton, 1968: A theory of the quasi-biennial oscillation. *J. Atmos. Sci.*, **25,** 1095–1107.

Lipps, F. B., and R. S. Hemler, 1982: A scale analysis of deep moist convection and some related numerical calculations. *J. Atmos. Sci.*, **39,** 2192–2210.

——, and ——, 1986: Numerical simulation of deep tropical convection associated with large-scale convergence. *J. Atmos. Sci.*, **43,** 1796–1816.

——, and ——, 1988: Numerical modeling of a line of towering cumulus on day 226 of GATE. *J. Atmos. Sci.*, **43,** 1796–1816.

——, and ——, 1991: Numerical modeling of a midlatitude squall line: Features of the convection and vertical momentum fluxes. *J. Atmos. Sci.*, **48,** 1909–1929.

Lord, S. J., H. E. Willoughby, and J. M. Piotrowicz, 1984: Role of parameterized ice-phase microphysics in an axisymmetric, nonhydrostatic tropical cyclone model. *J. Atmos. Sci.*, **41,** 2836–2848.

McLatchey, R. A., R. W. Fenn, J. E. A. Selby, F. E. Volz, and J. S. Garing, 1972: *Optical Properties of the Atmosphere.* AFCRL-72-0497, Hanscom Air Force Base, Bedford, MA, 110 pp.

Manabe, S., and R. F. Strickler, 1964: Thermal equilibrium of the atmosphere with a convective adjustment. *J. Atmos. Sci.*, **21,** 361–385.

——, and R. T. Wetherald, 1967: Thermal equilibrium of the atmosphere with a given distribution of relative humidity. *J. Atmos. Sci.*, **24,** 241–259.

——, J. Smagorinsky, and R. F. Strickler, 1965: Simulated climatology of a general circulation model with a hydrologic cycle. *Mon. Wea. Rev.*, **93,** 769–798.

Nakajima, K., and T. Matsuno, 1988: Numerical experiments concerning the origin of cloud clusters in the tropical atmosphere. *J. Meteor. Soc. Japan,* **66,** 309–329.

Neelin, J. D., I. M. Held, and K. H. Cook, 1987: Evaporation–wind feedback and low-frequency variability in the tropical atmosphere. *J. Atmos. Sci.*, **44,** 2341–2348.

Piacsek, S. A., and G. P. Williams, 1970: Conservation properties of convection difference schemes. *J. Comput. Phys.*, **6,** 392–405.

Plumb, R. A., 1977: The interaction of two internal waves with the mean flow: implications for the theory of the quasi-biennial oscillation. *J. Atmos. Sci.*, **34,** 1847–1858.

Ramanathan, V., and J. A. Coakley, Jr., 1978: Climate modeling through radiative-convective models. *Rev. Geophys. Space Phys.*, **16,** 465–489.

Ramaswamy, R., and J. T. Kiehl, 1985: Sensitivities of the radiative forcing due to large loadings of smoke and dust aerosols. *J. Geophys. Res.*, **90,** 5597–5613.

Sarachik, E. S., 1978: Tropical sea surface temperature: an interactive one-dimensional atmosphere–ocean model. *Dyn. Atmos. Oceans,* **2,** 2621–2641.

Saravanan, R., 1990: A multiwave model of the quasi-biennial oscillation. *J. Atmos. Sci.*, **47,** 2465–2474.

Slingo, A., 1989: A GCM parameterization for the shortwave radiative properties of water clouds. *J. Atmos. Sci.*, **46,** 1419–1427.

Somerville, R. C. J., and C. A. Remer, 1984: Cloud optical thickness feedbacks in the CO_2 climate problem. *J. Geophys. Res.*, **89,** 9668–9672.

Stephens, G. L., 1978: Radiation profiles in extended water clouds, II: Parameterization schemes. *J. Atmos. Sci.*, **35,** 2123–2132.

——, and P. J. Webster, 1981: Clouds and climate: Sensitivity of simple systems. *J. Atmos. Sci.*, **38,** 235–247.

Sui, C. H., K. M. Lau, W. K. Tao, and J. Simpson, 1993: The tropical water and energy cycles in a cumulus ensemble model. Part I: Equilibrium climate. *J. Atmos. Sci.*, in press.

Tao, W.-K., and J. Simpson, 1989: Modeling study of a tropical squall-type convective line. *J. Atmos. Sci.*, **46,** 177–202.

——, ——, and S.-T. Soong, 1987: Statistical properties of a cloud ensemble. A numerical study. *J. Atmos. Sci.*, **44,** 3175–3187.

Xu, K.-M., and S. K. Krueger, 1991: Evaluation of cloudiness parameterization using a cumulus ensemble model. *Mon. Wea. Rev.*, **119,** 342–367.